



Na_3PO_4 assistant dispersion of nano- CaCO_3 template to enhance electrochemical interface: N/O/P co-doped porous carbon hybrids towards high-performance flexible supercapacitors

Yanliang Wen ^a, Xiaoguang Liu ^a, Xin Wen ^{a,*}, Xuecheng Chen ^{a,**}, Karolina Szymańska ^a, Renata Dobrzańska ^b, Ewa Mijowska ^a

^a Department of Nanomaterials Physicochemistry, Faculty of Chemical Technology and Engineering, West Pomeranian University of Technology Szczecin, Piastów Ave. 42, 71-065, Szczecin, Poland

^b Faculty of Maritime Technology and Transport, West Pomeranian University of Technology Szczecin, Al. Piastów 41, 71-065, Szczecin, Poland

ARTICLE INFO

Keywords:

Carbon hybrids
Heteroatom doped carbon
Supercapacitor
Energy storage

ABSTRACT

Recently porous carbon hybrids have attracted ever-increasing attention as electrode materials for supercapacitors, but it remains a great challenge to simultaneously control their pore structure and element composition with optimal electrochemical performances. Herein, Na_3PO_4 assistant dispersion of nano- CaCO_3 template in egg white was proposed to fabricate nitrogen/oxygen/phosphorus (N/O/P) co-doped 3D hierarchical porous carbon hybrids. The as-prepared carbon exhibited a high surface area ($2576 \text{ m}^2 \text{ g}^{-1}$), well-balanced pore size distribution with a large micropore volume ($0.77 \text{ cm}^3 \text{ g}^{-1}$) and multi-heteroatoms doped carbon skeleton (3.9% of N, 12.2% of O and 4.1% of P). These physicochemical advantages were synergistically beneficial to supercapacitive performances: an ultrahigh capacitance of 452 F g^{-1} at 0.5 A g^{-1} in 6 M KOH electrolyte and excellent stability of 92.4% capacitance retention after 10000 cycles at 10 A g^{-1} . The energy density was 22.6 Wh kg^{-1} at the power density of 225.0 W kg^{-1} in the neutral electrolyte of 1 M Li_2SO_4 . Especially, a flexible symmetric solid-state supercapacitor was assembled, which delivered a high capacitance (166 F g^{-1}) and excellent flexibility (86.3% capacitance retention) with bending angles to 180° . Thus, this work provides a cost-effective strategy to fabricate multi-element co-doped 3D hierarchical porous carbon and expand its application for flexible energy storage devices.

1. Introduction

Supercapacitors are emerging energy storage devices that have attracted intense attention by virtue of their high power density, short charging time and outstanding cyclic stability [1–6]. However, the relatively low specific capacitance and poor energy density are still the main obstacles for their wide commercial applications. The performance of a supercapacitor is mainly dominated by its electrode materials [7,8]. In principle, the capacitance can be attributed to quick charge accumulation in the interface of electrode-electrolyte, resulting in a fast charge-discharge process. Ideally, to enhance electrochemical interface activity, the electrode materials should have large specific surface area (SSA) for charge storage, well-balanced hierarchical porosity (micro-, meso- and macro-pores) for fast ion transport and diffusion, high

electrical conductivity for efficient electron transfer and good wettability for promoting the pore accessibility to electrolyte [9,10]. Thus, to achieve high-performance supercapacitors, it is extremely imperative to design and synthesize electrode materials with rational pore structure and element composition for meeting the requirements of ideal electrodes.

Recently porous carbons are regarded as promising electrode materials due to their good conductivity, abundant morphology and tunable surface properties by doping and/or surface functionalization [11–13]. In this regard, numerous strategies have been developed to control the pore size distribution of porous structure, such as hydrothermal reaction [14], self-assembly [15], molten-salt route [16], electrophoretic deposition [17], hard/soft templates [18], etc. Especially, the hard-template method is of particular interest because it is robust and reproducible,

* Corresponding author.

** Corresponding author.

E-mail addresses: hgwenxin@126.com (X. Wen), xchen@zut.edu.pl (X. Chen).

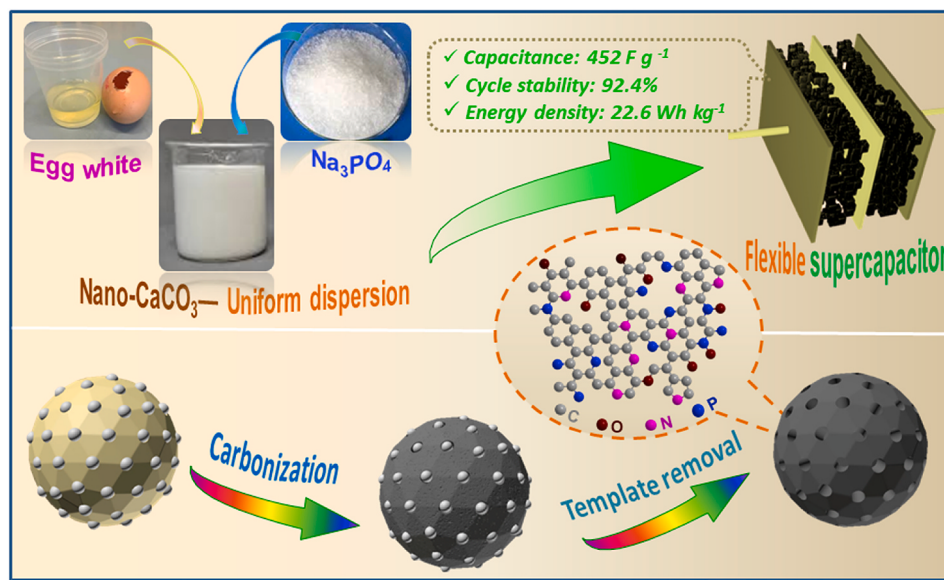


Fig. 1. A schematically synthetic process of multi-heteroatom co-doped 3D hierarchical porous carbon for supercapacitor.

where the template itself is embedded in the carbon precursor to generate porous structure after template removal [19]. Various efforts have been made to manufacture porous carbon materials by template method from zeolites, nickel hydroxide, silica spheres, zinc oxide, calcium carbonate, etc. [20–22]. However, the pore size distribution is difficult to control because of the strong aggregation tendency of nanosized templates in carbon precursors, resulting in the presence of some oversized macro-pores in the resultant hierarchical porous carbons.

Besides pore size distribution, the elemental composition of porous carbons also makes a great contribution to the electrochemical properties of supercapacitors. It is well-known that the heteroatoms of nitrogen (N), oxygen (O), phosphorus (P), boron (B), and sulfur (S) are commonly pinned onto nanostructured carbon surfaces, which induce pseudo-faradaic processes with a substantial increase of total capacitance [19, 23–25]. In this case, biomasses are viewed as a promising natural carbon precursor due to their wide availability and sustainability [26, 27]. More importantly, they contain abundant heteroatoms that can be in-situ doped into carbon matrices during carbonization processes. Up to now, a series of raw biomass materials (mainly include plants and animals) have been converted into porous carbons for supercapacitor electrodes, such as willow catkin [28], cashmere [29], bagasse [30], eggshell membrane [31], human hair [32], shiitake mushroom [33], auricularia [34], lessonia nigrescens [35], etc. Nevertheless, it is still a challenge to simultaneously control pore distribution and multi-element doping of nanostructured carbons for achieving the optimized electrochemical performances in supercapacitors.

In this study, Na₃PO₄ assistant dispersion of nano-CaCO₃ template was proposed to fabricate heteroatoms co-doped hierarchical porous carbon hybrids from biomass. It is noted that nano-CaCO₃ was used as both a template and a pore-forming agent due to its thermal decomposition to produce CaO and CO₂ during annealing [36, 37]. Meanwhile, Na₃PO₄ was acted as a phosphorus source and also an efficient dispersant for nano-CaCO₃ in egg white. As schematically shown in Fig. 1: firstly, egg white (nitrogen-rich protein) and Na₃PO₄ were added into CaCO₃ aqueous dispersion, then the composites were converted into porous carbons via carbonization and template removal. The obtained carbon exhibited a high specific surface area of 2576 m² g⁻¹, well-balanced pore size distribution and multi-heteroatoms doping (N, P and O). Benefiting from these advantageous features, this porous carbon delivered high specific capacitance (452 F g⁻¹ at 0.5 A g⁻¹), good cyclic ability (92.4% capacitance retention after 10000 cycles) and high

energy density (22.6 Wh kg⁻¹ at the power density of 225.0 W kg⁻¹). Moreover, the as-developed flexible sandwiched solid-state supercapacitor exhibited a high capacitance of 166 F g⁻¹ and excellent flexibility of 86.3% capacitance retention with the bending angle of 180°. This work provides a facile strategy to fabricate porous carbon with rational pore size distribution and multi-heteroatoms doping. Meanwhile, it exploits exciting applications in the field of energy storage.

2. Experimental section

2.1. Materials

Eggs were purchased from a local supermarket (Carrefour, Szczecin, Poland). Nano-CaCO₃ was bought from Sinopharm Chemical Reagent Co. Ltd. TEM images showed its average diameter of approximately 35 nm (Fig. S1 in Supporting Information). Trisodium phosphate (Na₃PO₄) was bought from Sigma-Aldrich. All the chemical reagents were of analytical grade and used as received without any further purification.

2.2. Synthesis of hierarchical porous carbons

The synthesis process for hierarchical porous carbon is illustrated in Fig. S2. Firstly, nano-CaCO₃ (2.0 g) was dissolved in 100 ml deionized water with the assistance of a magnetic stirrer for 1 h. Na₃PO₄ (5.0 g) was added into the above dispersion with vigorous sonication for 10 min. About 30 ml of egg white was collected from one egg, then it was gradually added into the dispersed mixture and stirred for 2 h. Subsequently, the mixture was heated at 60 °C in the air until it became a dry white solid. Finally, the carbonization was carried out in a horizontal quartz tube at 800 °C with a heating rate of 3 °C min⁻¹ for 2 h under N₂ atmosphere. After that, the furnace was cooled down to room temperature with a rate of 4 °C min⁻¹. The obtained sample was purified by diluted hydrofluoric acid and then dried in a vacuum oven at 60 °C for 12 h. The egg white/Na₃PO₄ derived carbon with the nano-CaCO₃ template was denoted as EW-P-T. As reference samples, pure egg white (EW) and egg white with nano-CaCO₃ without Na₃PO₄ (EW-T) were synthesized under the same conditions, respectively.

2.3. Materials characterization

Field-emission scanning electron microscopy (SEM) was applied to observe the carbon morphology on an XL30ESEM-FEG scanning electron

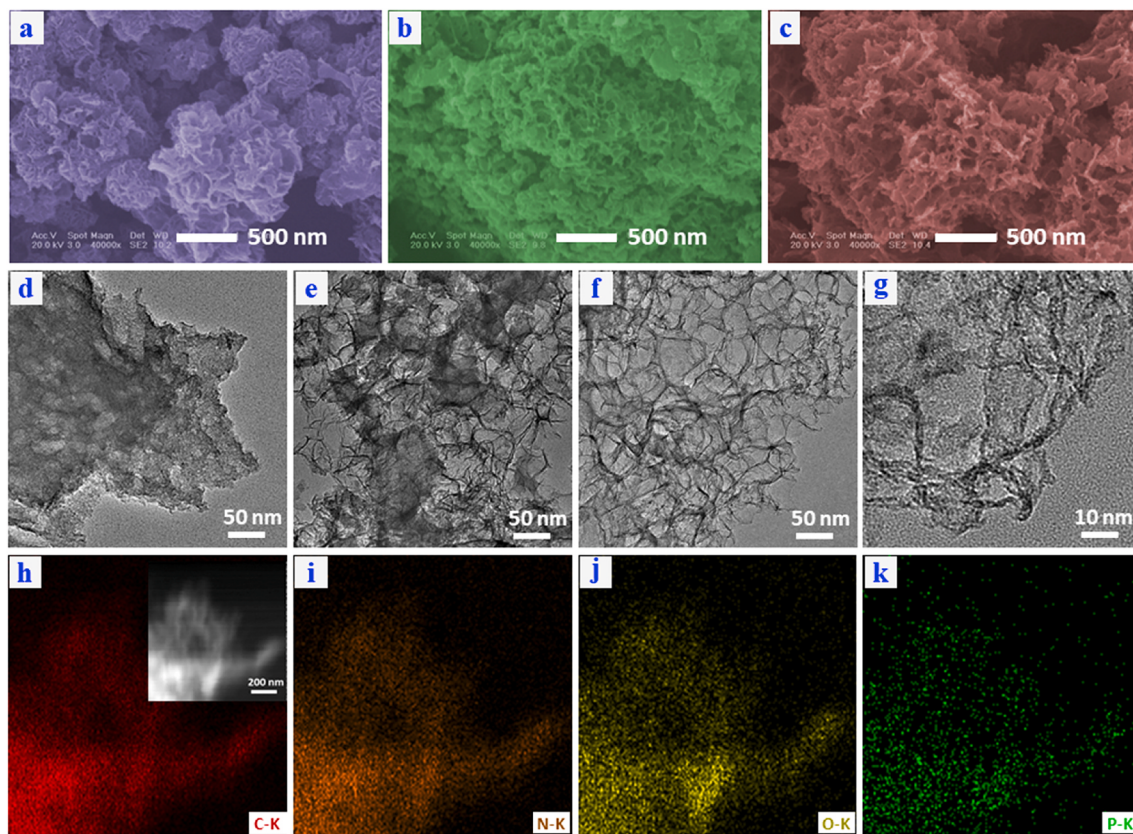


Fig. 2. SEM images of (a) EW, (b) EW-T and (c) EW-P-T; TEM images of (d) EW, (e) EW-T and (f, g) EW-P-T; EDX elemental mapping images of (h) C, (i) N, (j) O and (k) P for EW-P-T.

microscopy with an acceleration voltage of 20 kV. Before SEM observation, a thin gold foil of 20 nm was coated on the surfaces of samples. Transmission electron microscopy (TEM) was performed on a Tecnai F30 transmission electron microscope at 200 kV accelerating voltage. EDS mapping was carried out in the energy-dispersive X-ray spectroscopy (EDAX, Mahwah, NJ, USA). X-ray diffraction (XRD) patterns were collected on an X'Pert Philips Diffractometer with Cu K α radiation ($\lambda = 1.5406 \text{ \AA}$) from the Co radiation. Raman scattering spectra were determined via a Raman spectrometer with the excitation beam wavelength of 785 nm (Renishaw, New Mills Wotton-under-Edge, UK). Thermogravimetric analysis (TGA) was performed on a DTA-Q600 SDT TA Instrument. The ramp rate was $10 \text{ }^{\circ}\text{C min}^{-1}$ at the air flow within the temperature range of $25\text{--}800 \text{ }^{\circ}\text{C}$. X-ray photoelectron spectroscopy (XPS) was carried out on a VG ESCALAB MK II spectrometer with Al K α radiation under the operating conditions of 10.0 kV and 10 mA. The nitrogen adsorption/desorption measurement was employed to evaluate the specific surface areas (SSA) and the pore size distribution (PSD) on a Quantachrome Autosorb-1C-MS analyzer. Brunauer-Emmett-Teller (BET) and non-local density functional theory (NLDFT) were used to calculate the SSA_{BET} and PSD of the resulted carbon materials, respectively. All the samples were heated at $200 \text{ }^{\circ}\text{C}$ for 12 h to degas prior to the nitrogen adsorption/desorption measurements.

2.4. Electrochemical measurements

The electrochemical performances of carbons were recorded by both a symmetric three-electrode system and a two-electrode system on the EC-LAB VMP3 multichannel generators (BioLogic Science Instruments, France). In the three-electrode system, the aqueous electrolyte of 6 M KOH was used. The active material (80 wt%), 10 wt% carbon black and 10 wt% poly(tetrafluoroethylene) were mixed and ground in acetone to form an evenly dispersed carbon slurry, then it was coated onto a

collector (nickel foam, $1 \times 1 \text{ cm}^2$). Subsequently, the coated tablet was pressed at 6 MPa followed by vacuum drying at $80 \text{ }^{\circ}\text{C}$ for 12 h. The loading of active substance for each working electrode was 1.0 mg. A piece of nickel foam with a large area was used as the counter electrode and a saturated calomel electrode was served as the reference electrode.

The cyclic voltammetry (CV) and galvanostatic charge-discharge (GCD) curves were conducted in the potential window from 0 to -1V . The corresponding scan rate varied from 1 to 200 mV s^{-1} and the current density increased from 0.5 to 20 A g^{-1} . The electrochemical impedance spectroscopy (EIS) was also analyzed over a frequency range of 100 kHz to 0.1 Hz at open potential with a current amplitude of 5 mV. In a three-electrode system, the gravimetric specific capacitance was calculated from the integral area of the CV curve based on Equation (1):

$$C(\text{F/g}) = \frac{1}{2} \times \frac{1}{m \times \Delta v \times s} \times \left(\int_{v_0}^v idv + \int_v^{v_0} idv \right) \quad (1)$$

or according to Equation (2) from GCD curve:

$$C(\text{F/g}) = \frac{I \Delta t}{m \Delta v} \quad (2)$$

where m , Δv , s , I , Δt and the integral part are the mass loading (mg), the voltage window (V), the scan rate (mV s^{-1}), the current density (mA), the discharge time (s) and the area of CV curve.

The ion diffusion coefficient (D) was calculated based on the EIS data according to the following Equations (3) and (4):

$$D = \frac{R^2 T^2}{2A^2 n^4 C^2 F^4 \sigma^2} \quad (3)$$

$$Z = R_S + R_{CT} + \sigma \omega^{-0.5} \quad (4)$$

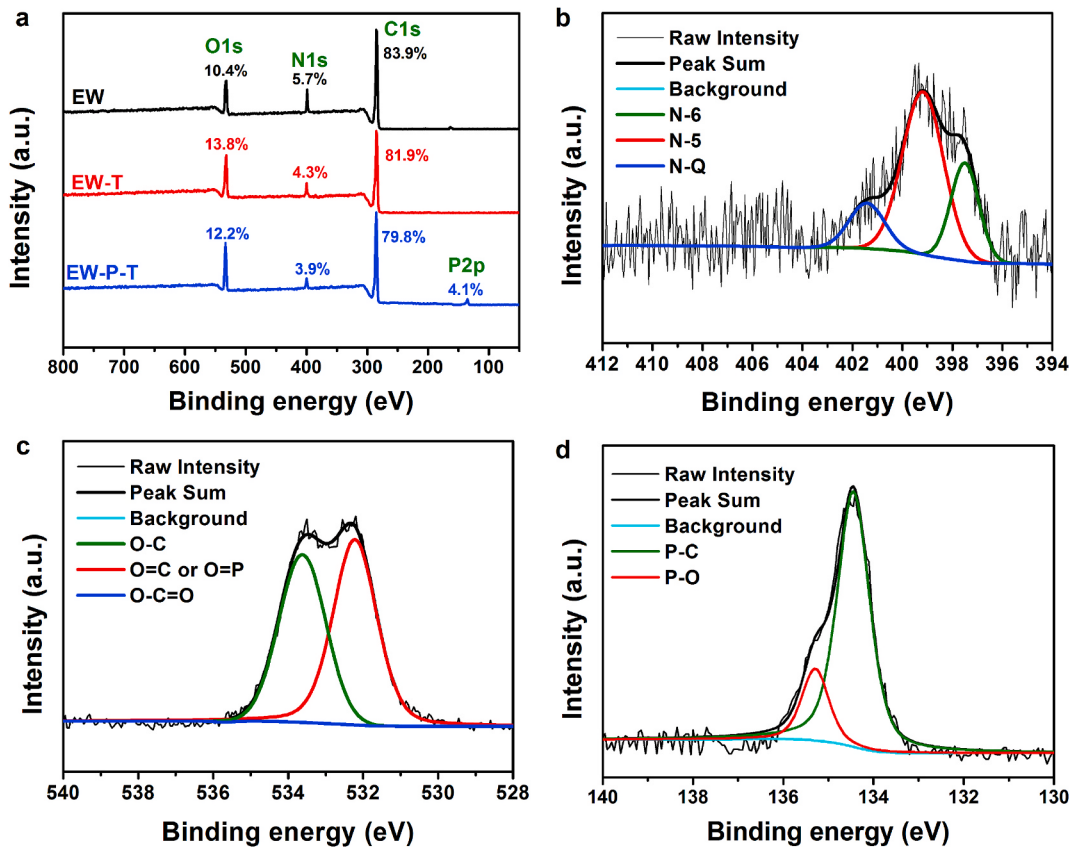


Fig. 3. (a) XPS survey spectra and relative atomic percentages of elements for egg white derived carbons; High-resolution XPS plots of (b) N1s, (c) O1s and (d) P2p for EW-P-T.

where R is the gas constant, T is the temperature (K), A is the effective area of electrode, n is the number of electrons, C is the concentration of transferred ion, F is the Faraday's constant and σ is the Warburg factor, $\omega^{-0.5}$ is the square root of angular frequency in the low-frequency region [38].

In the two-electrode system, 6 M KOH and 1 M Li₂SO₄ were used as electrolytes. The preparation procedure was the same as that in the three-electrode system but used round nickel foam with a diameter of 1.0 cm as the current collector. Each electrode also contained 1.0 mg of active material. The separator was a piece of glassy fibrous paper (Whatman GF/G). The supercapacitors were fabricated into a Swagelok type cell. According to the mechanism of double-layer supercapacitors, the electrochemical values were calculated by Equations (5)–(8). The specific capacitance from CV curves based on Equation (5):

$$C(F/g) = \frac{1}{m \times \Delta V \times s} \times \left(\int_{v_0}^V idv + \int_V^{v_0} idv \right) \quad (5)$$

The specific capacitance calculated from GCD curves by Equation (6):

$$C(F/g) = \frac{2I\Delta t}{m\Delta V} \quad (6)$$

Energy density and power density were calculated according to the equations (7) and (8) respectively:

$$E(\text{Wh/kg}) = \frac{C\Delta V^2}{8 \times 3.6} \quad (7)$$

$$P(\text{kW/kg}) = \frac{E \times 3.6}{\Delta t} \quad (8)$$

Where all related physical quantities are the same as the previous description in the three-electrode system.

The polyvinyl acetate (PVA)/LiCl gel acted as the electrolyte to fabricate a solid-state flexible supercapacitor. It was obtained by adding 3.0 g PVA, 3.0 g LiCl into 30 mL deionized water through magnetic stirring, ultrasonication and heating at 95 °C for 1 h. After it became clear, the obtained PVA solution gel was naturally cooled down to room temperature. Subsequently, two identical pieces of carbon cloth were coated with a mixture of EW-P-T (10.0 mg), carbon black (1.0 mg) and 5% PTFE (0.1 mL). Then, the two electrodes were immersed into the gel for 15 min. Then they were assembled into a sandwiched supercapacitor using a cellulose separator with a thickness of 20 μm. The flexible solid-state supercapacitor was obtained after the gel solidified at room temperature for 12 h.

3. Results and discussion

3.1. Characterization of egg white derived carbons

3.1.1. Analysis of morphology and microstructure

The morphology of egg white derived carbons was characterized by SEM and TEM. As defined previously, the EW, EW-T and EW-P-T represent the carbon from neat egg while, egg while with nano-CaCO₃ template and egg while/Na₃PO₄ with the nano-CaCO₃ template, respectively. The EW exhibited regular spherical morphology formed by wrinkled carbon flakes (Fig. 2a). Notably, with nano-CaCO₃ as the template, the carbon of EW-T formed a continuous and sponge-like tridimensional structure (Fig. 2b). These macro-pores might be the voids after the removal of the nano-CaCO₃ template. For EW-P-T, the macro-porous structure became more uniform due to the assistance of Na₃PO₄ as a dispersant (Fig. 2c).

Table 1

Summary of XPS peak analysis for egg white derived carbons.

Samples	N1s (%)			O1s (%)			P2p (%)	
	N-6	N-5	N-Q	O-C	O=C/ O=P	O-C=O	P-C	P-O
EW	18.9	73.1	8.0	37.1	46.8	16.1	—	—
EW-T	22.2	64.3	13.5	46.2	53.6	0.2	—	—
EW-P-T	25.0	60.4	14.6	46.0	53.8	0.2	81.3	18.7

Furthermore, their nanostructures were observed by TEM. The EW was composed of thick carbon flakes, while the EW-T exhibited ultrathin nanosheets (Fig. 2d and 2e). Like the EW-T, the EW-P-T presented a 3D framework, but these nanosheets were thinner and more uniform (Fig. 2f). Especially, the high-resolution TEM for EW-P-T clearly showed highly porous nature (abundant mesopores were noticeable; micropores were evaluated by N₂ adsorption–desorption measurement later). Thus, it is believed that the EW-P-T with hierarchical porous structure is helpful in fast access/transport/diffusion of electrolyte ions, resulting in

high-performance of supercapacitors. Meanwhile, elemental mapping images displayed the uniform distribution of nitrogen/oxygen/phosphorus (N/O/P) atoms in the carbon skeleton of EW-P-T (Fig. 2h–k), suggesting the formation of multi-heteroatom co-doped carbon lattice. As a comparison, the elemental mappings for EW and EW-T were also performed (Fig. S3). No P element was detected in their carbon skeletons, indicating that the P presence in EW-P-T came from Na₃PO₄.

3.1.2. Analysis of elementary composition

XPS was used to investigate the surface elemental composition of egg white derived carbons. It is helpful to analyze the bonding configurations and doping degree of the heteroatoms. The full XPS survey spectra of them are shown in Fig. 3a. The peaks at 285, 400, and 532 eV regions were present in all plots, which were assigned to C1s, N1s, and O1s, respectively. The EW contained 83.9% C, 5.7% N and 10.4% O. In the case of EW-T with nano-CaCO₃ as template, the content of N decreased to 4.3% while that of O increased to 13.8%, which were ascribed to the etching effect of CaCO₃ (the detailed chemical reactions were discussed

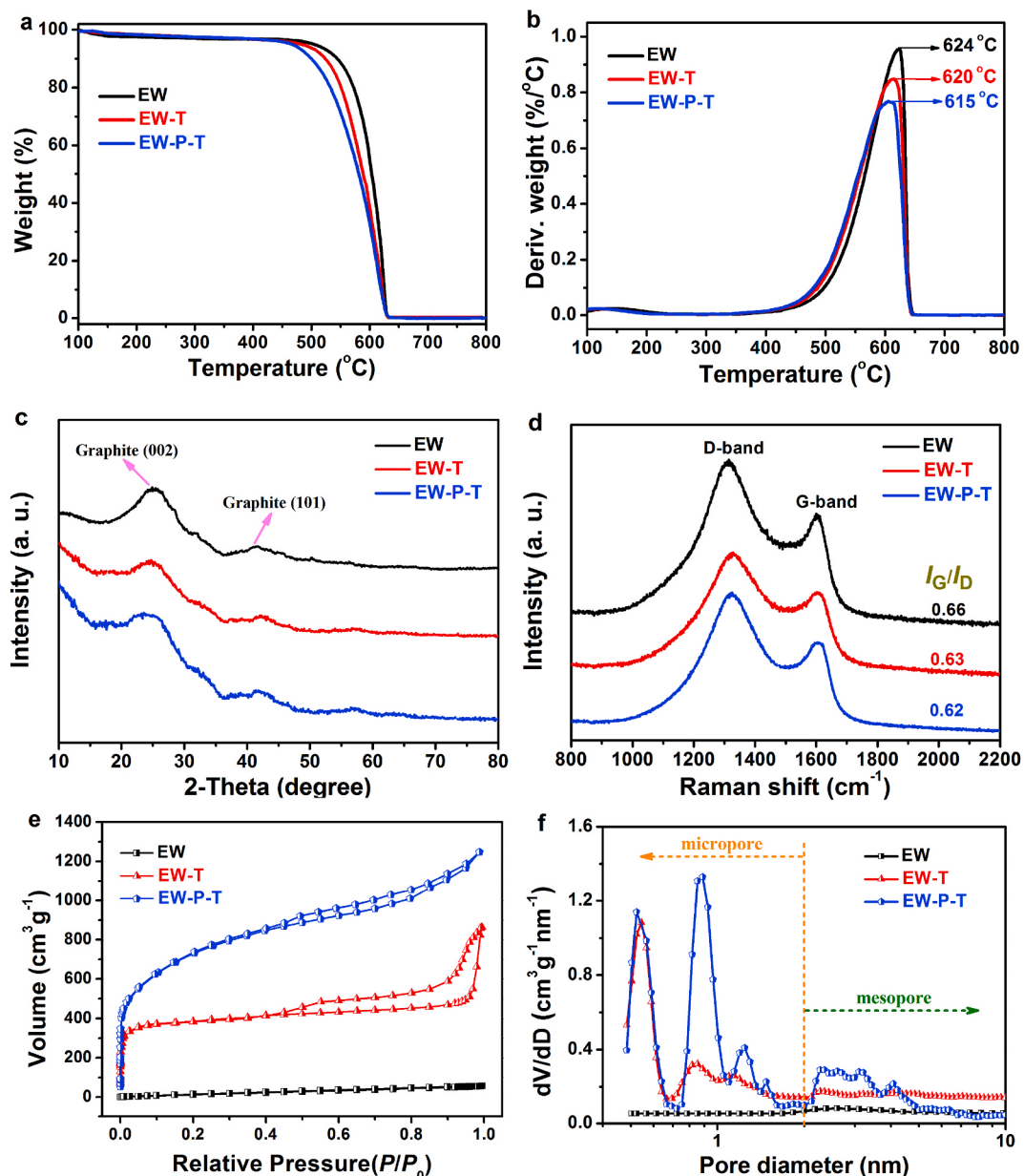


Fig. 4. (a) TGA curves, (b) DTG curves, (c) XRD patterns, (d) Raman spectra, (e) N₂ adsorption-desorption isotherms, and (f) pore size distribution of carbons.

Table 2Pore structure parameters from N₂ adsorption-desorption measurements.

Samples	S _{BET} ^a (m ² g ⁻¹)	V _{total} ^b (cm ³ g ⁻¹)	V _{micro} ^c (cm ³ g ⁻¹)	Pore distribution ^d (nm)
EW	75	0.09	0.01	2.63
EW-T	1487	1.34	0.50	0.57/0.87/2.27
EW-P-T	2576	1.93	0.77	0.55/0.87/1.25/2.35/4.08

^a Specific surface area derived from the Multi-Point BET method.^b Total pore volume derived from density functional theory (DFT).^c Microporous volume calculated via DFT.^d Pore distribution calculated via DFT method.

later). However, for the sample of EW-P-T with the further addition of Na₃PO₄, there was a slight reduction for N (3.9%) and O (12.2%), but the P as a new element was detected with 4.2% content. As far as we know, it is quite a high value of P content in comparison with previous reports on P-doped carbon materials (Table S1).

The incorporation of heteroatoms into carbon lattice for the fabricated samples was further confirmed by high-resolution XPS spectra. As shown in Fig. 3b and Table 1, the N1s spectrum of EW-P-T was fitted to pyridinic-N (N-6, 25.0%), pyrrolic-N (N-5, 60.4%) and quaternary-N (N-Q, 14.6%), respectively [39]. Compared to the other two samples (Fig. S4 and Table 1), the EW-P-T exhibited higher values of N-6 and N-Q. Meanwhile, with nano-CaCO₃ as the template in EW-T and EW-P-T, the percent of O-C and O=C/O=P greatly increased, but the O-C=O became negligible with only 0.2% (Fig. 3c and Table 1). In Fig. 3d, the P2p of EW-P-T was separated into two featured peaks at 134.4 eV (P-C) and 135.1 eV (P=O). More importantly, the content of P-C was 81.3%, which is much higher than that of P=O (18.7%) (Table 1). This result verified the successful doping of P heteroatoms into carbon lattice instead of the marginal area of carbon, which might be an important

factor resulting in high capacitances of supercapacitors. Meanwhile, it indicated that Na₃PO₄ was an efficient phosphorus source in the egg white system.

3.1.3. Purity, graphitization degree and pore structure

The purity and graphitic nature of the above carbon samples were evaluated by TGA in air atmosphere. According to TGA curves in Fig. 4a, the residues at 800 °C were near to zero, suggesting that no solid products from nano-CaCO₃ and Na₃PO₄ remained in the carbon hybrids after the purification treatment. From the DTG curves in Fig. 4b, a gradually decreased trend with shifting to low temperature present. The maximum oxidation temperature (*T*_{max}) was 624, 620, and 615 °C for EW, EW-T and EW-P-T, respectively, indicating that the carbon skeleton exhibited more disordered graphitized structure and contained more defects (heteroatoms, functional groups, pores, etc.). Notably, this trend was well consistent with the above TEM and XPS results.

The phase structure of as-prepared carbon materials was further characterized by XRD and Raman. As presented in Fig. 4c, there were two strong peaks at ~24° and 43°, which were assigned to the (002) and (101) reflections of graphitic carbon [40,41]. In XRD patterns of EW and EW-P-T, there was no obvious difference in the (101) peak. However, the intensity of (002) gradually decreased, indicating that the nano-CaCO₃ and Na₃PO₄ weakened the graphitic degree of carbon materials. Moreover, Fig. 4d showed the Raman spectra of the samples. Generally, the peak centered at 1352 cm⁻¹ (D-band) is a reflection of the defects and disorder of carbon materials, while another peak located at 1585 cm⁻¹ (G-band) is assigned to the vibration of all sp² hybridized carbon atoms both in chains and rings [42]. The intensity ratio of G-band to D-band values (*I*_G/*I*_D) was in the order of EW (0.66) > EW-T (0.63) > EW-P-T (0.62), suggesting that the formation of more defects and disorder fractions upon using the nano-CaCO₃ as the template. This character would be beneficial to improve the wettability of electrode material and

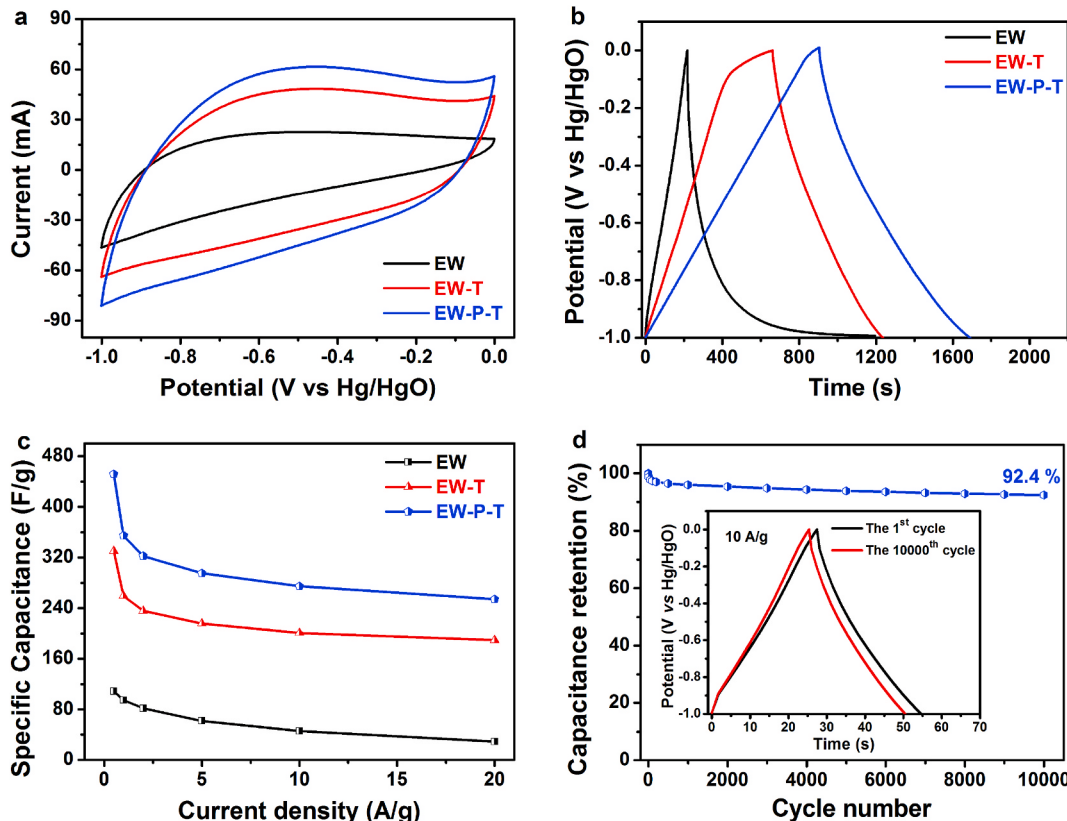


Fig. 5. Electrochemical properties in 6 M KOH three-electrode system: (a) CV curves at 200 mV s⁻¹; (b) GCD curves at 0.5 A g⁻¹; (c) Specific capacitance at various current densities; (d) Cycle stability of EW-P-T at 10 A g⁻¹, the inset shows the 1st and 10000th cycles of GCD curves).

Table 3

Comparison of the electrochemical performances of carbons in the three-electrode system.

Carbon sources	Activating agent /template	SSA_{BET} ($m^2 g^{-1}$)	Electrolyte	Current density ($A g^{-1}$)	Capacitance ($F g^{-1}$)	Ref.
Wheat flour	SiO ₂	875	6 M KOH	0.5	179	[43]
Beans shells	KOH	655	6 M KOH	0.5	202	[44]
Melamine/glucose	CaCO ₃	414	6 M KOH	0.5	212	[45]
Pomelo mesocarps	CaCl ₂	975	2 M KOH	0.5	245	[46]
Lignin	KOH	870	6 M KOH	0.5	245	[47]
Methylnaphthalene oil	KOH/CaCO ₃	1136	6 M KOH	0.05	286	[48]
Almond shells	KOH	373	6 M KOH	1	286	[49]
Eggshell membrane	Air	221	1 M KOH	0.2	297	[31]
Willow catkin	KOH	1533	6 M KOH	0.5	298	[28]
Bamboo	KOH	1472	6 M KOH	0.1	301	[50]
Shiitake mushroom	H ₃ PO ₄ /KOH	2988	6 M KOH	1	306	[33]
Resorcinol/formaldehyde	SiO ₂	1500	6 M KOH	1	310	[51]
Bagasse	KOH	2296	6 M KOH	0.5	320	[30]
Polyvinylidene fluoride	SiO ₂	1431	6 M KOH	0.5	337	[52]
Human hair	KOH	1306	6 M KOH	1	340	[32]
Shrimp shell	KOH/CaCO ₃	1343	6 M KOH	0.05	348	[53]
Resorcinol resin	KOH/CaCO ₃	1525	6 M KOH	1	350	[36]
Cashmere	KOH	1358	6 M KOH	0.5	363	[29]
Fungus	KOH	1103	6 M KOH	0.5	374	[54]
Protein	SiO ₂	806	1 M H ₂ SO ₄	0.5	390	[55]
Poly(2-thiophenemethanol)	SiO ₂	792	6 M KOH	0.5	420	[56]
Phenolic resin	SiO ₂	922	6 M KOH	0.5	433	[57]
Egg-white	Nano-CaCO ₃	2576	6 M KOH	0.5	452	This work

promote the access of electrolyte ions, resulting in high electrochemical performances of supercapacitors.

The pore distribution and specific surface area (S_{BET}) were analyzed by N₂ adsorption–desorption measurements, and their detailed parameters were summarized in Table 2. As depicted in Fig. 4e, the EW was typical II sorption isotherm, indicating that it was almost a non-porous structure. However, the other two samples exhibited similar I/IV

sorption isotherms, giving steep curves at low relative pressures of $P/P_0 < 0.1$ and hysteresis loops at the P/P_0 of 0.5–1.0, which suggested that the carbons prepared by template method consisted of abundant micropores and mesopores. Notably, the non-coincident shape of isotherms at the high relative pressure ($P/P_0 \geq 0.9$) implied the existence of lots of macropores in the EW-T, which might be attributed to the voids of nano-CaCO₃ aggregates after template removal. This further confirmed that

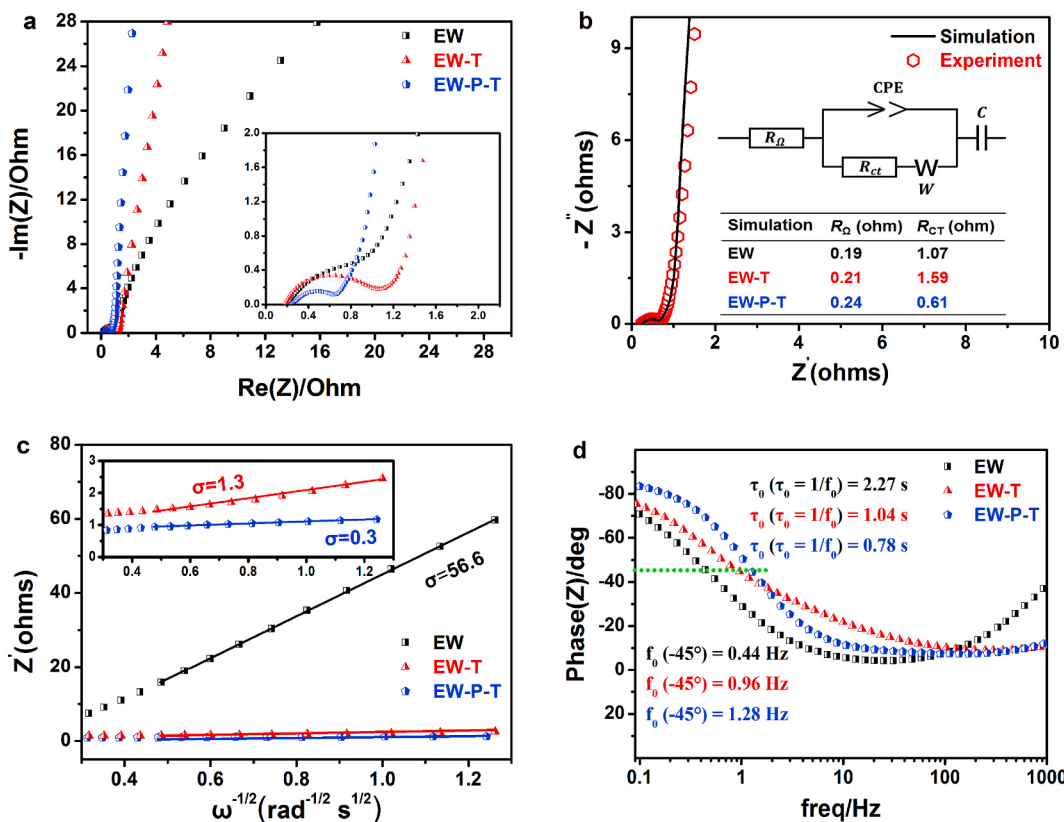


Fig. 6. (a) Nyquist plots of egg white derived carbons in 6 M KOH using a three-electrode system. (b) Experimental and simulative comparison of Nyquist plots for EW-P-T (the insets are an equivalent circuit diagram and the ohmic/charge transfer resistances); (c) The relationship between Z' and $\omega^{-1/2}$ at low-frequency region; (d) Bode phase plots.

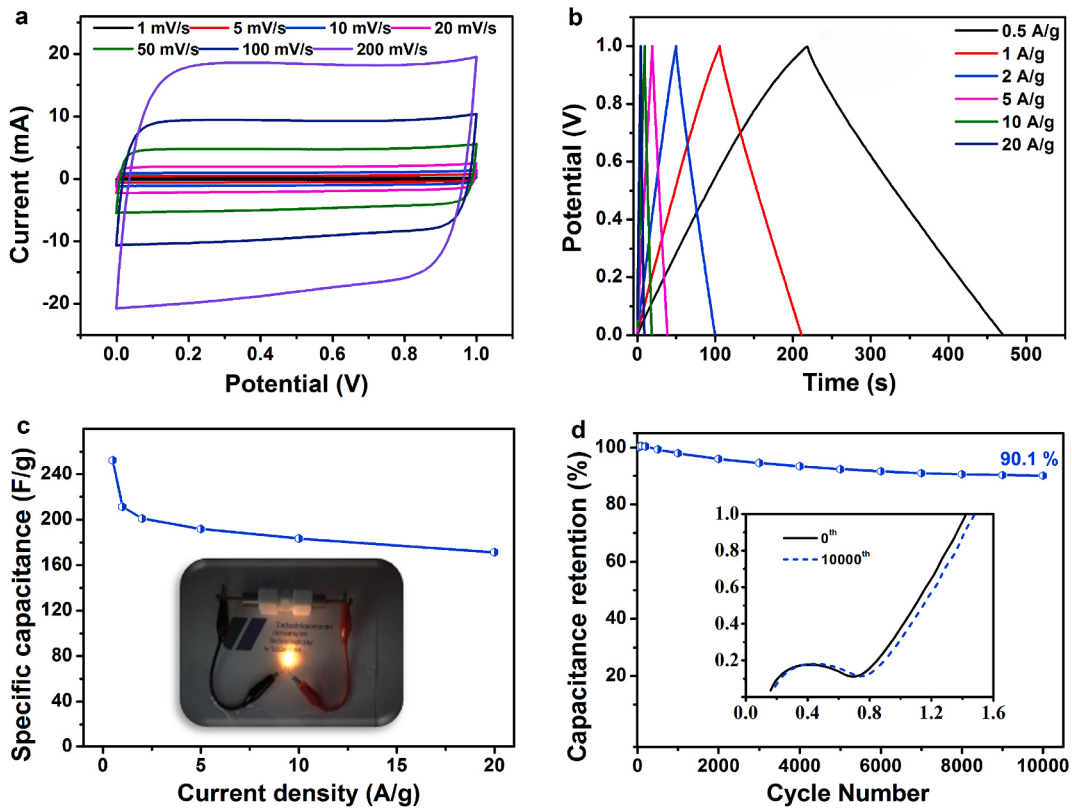


Fig. 7. Electrochemical properties of EW-P-T in two-electrode 6 M KOH system: (a) CV profiles from 1 to 200 mV s^{-1} ; (b) GCD curves from 0.5 to 20 A g^{-1} ; (c) Gravimetric specific capacitance over different current density (the inset shows a photograph of LED powered by EW-P-T); (d) The durability at 10 A/g for 10000 cycles.

Na_3PO_4 was an efficient auxiliary dispersant to prevent the aggregation of CaCO_3 nanoparticles, resulting in few macropores (or supermacropores) in the EW-P-T. The pore size distributions were shown in Fig. 4f. The pore size of EW-T was mainly focused on 0.57/0.87/2.27 nm, while EW-P-T exhibited much wider pore distribution at 0.55/0.87/1.25/2.35/4.08 nm.

As displayed in Table 2, the EW possessed the lowest values of S_{BET} ($75 \text{ m}^2 \text{ g}^{-1}$) and V_{total} ($0.09 \text{ cm}^3 \text{ g}^{-1}$). For the EW-T, the S_{BET} significantly enlarged to $1487 \text{ m}^2 \text{ g}^{-1}$ and its V_{total} increased to $1.34 \text{ cm}^3 \text{ g}^{-1}$, indicating that the nano- CaCO_3 template constructed a porous structure. Interestingly, the S_{BET} and V_{total} of EW-P-T reached $2576 \text{ m}^2 \text{ g}^{-1}$ and $1.93 \text{ cm}^3 \text{ g}^{-1}$ respectively, which can be ascribed to the synergistic effect of nano- CaCO_3 and Na_3PO_4 on adjusting the resultant pore structure. More importantly, the EW-P-T exhibited the highest micropore volume ($V_{\text{micro}} = 0.77 \text{ cm}^3 \text{ g}^{-1}$), which can provide abundant active sites for adsorbing electrolyte ions in supercapacitor. In brief, the EW-P-T exhibited unique advantages (the highest S_{BET} , the biggest V_{micro} and wider pore size distribution as well as N/O/P co-doped carbon lattice), which may make it as an extraordinary candidate of an electrode material for supercapacitors with promising electrochemical performances.

3.2. Evaluation of electrochemical performances

3.2.1. A three-electrode system in 6 M KOH

Electrochemical performances of egg white derived carbons were evaluated in a three-electrode system with 6 M KOH aqueous electrolyte. Fig. 5a showed CV curves at a high scan rate of 200 mV s^{-1} . They displayed quasi-rectangular shapes, indicating an ideal electrical double-layer capacitive behavior. Generally, the larger encircling area of a CV curve means the higher capacitance of supercapacitors. Among the three samples, the largest CV loop area of EW-P-T represented the highest specific capacitance. The humps in the CV curves might come from

redox reactions due to the heteroatoms doped in the carbon matrix, which can be contributed to the pseudo-capacitance of supercapacitors. Moreover, their GCD curves at 0.5 A g^{-1} were plotted in Fig. 5b. The EW-T exhibited a longer discharge time due to the formation of a porous pore structure via nano- CaCO_3 activation in comparison to EW. In the EW-P-T, when Na_3PO_4 is further added, the discharge time continued to increase to a higher value. More importantly, compared to EW and EW-T, the EW-P-T showed a better symmetrical triangular shape with no obvious IR drop, indicating an ideal capacitive behaviour with small internal resistance and excellent electrochemical reversibility for charge storage and delivery.

Fig. 5c showed the specific capacitance as a function of current density. At a low current density of 0.5 A g^{-1} , the EW-P-T depicted the specific capacitance as high as 452 F g^{-1} , which was much higher than the values in EW and EW-T as well as in those of previously reported carbon materials (Table 3). Even at a high current density of 20 A g^{-1} , the capacitance of EW-P-T remained at 274 F g^{-1} with the retention of 61% (The calculated values of specific capacitance at different current density are summarized in Table S2). It demonstrated the excellent rate capability and remarkable power capability of EW-P-T. In addition, the long-cycle performance was tested at a high current density of 10 A g^{-1} (Fig. 5d). It showed good durability of 92.4% capacitance retention after 10000 cycles. The inset curves displayed a little change between the first and the 10000th cycles, which directly confirmed the excellent electrochemical stability of EW-P-T as supercapacitors electrodes.

The electrochemical impedance spectroscopy (EIS) is useful to investigate the process of ion transport/charge transfer. In Fig. 6a, it was apparent that the EW-P-T had a smaller radius of the semicircle in the high-frequency region, which suggested the lower charge transfer resistance (R_{ct}). By expanding the vertical part of the plot to the X-axis, the EW-P-T exhibited the largest slope with a nearly vertical line, indicating the lowest equivalent series resistance (ESR). These typical

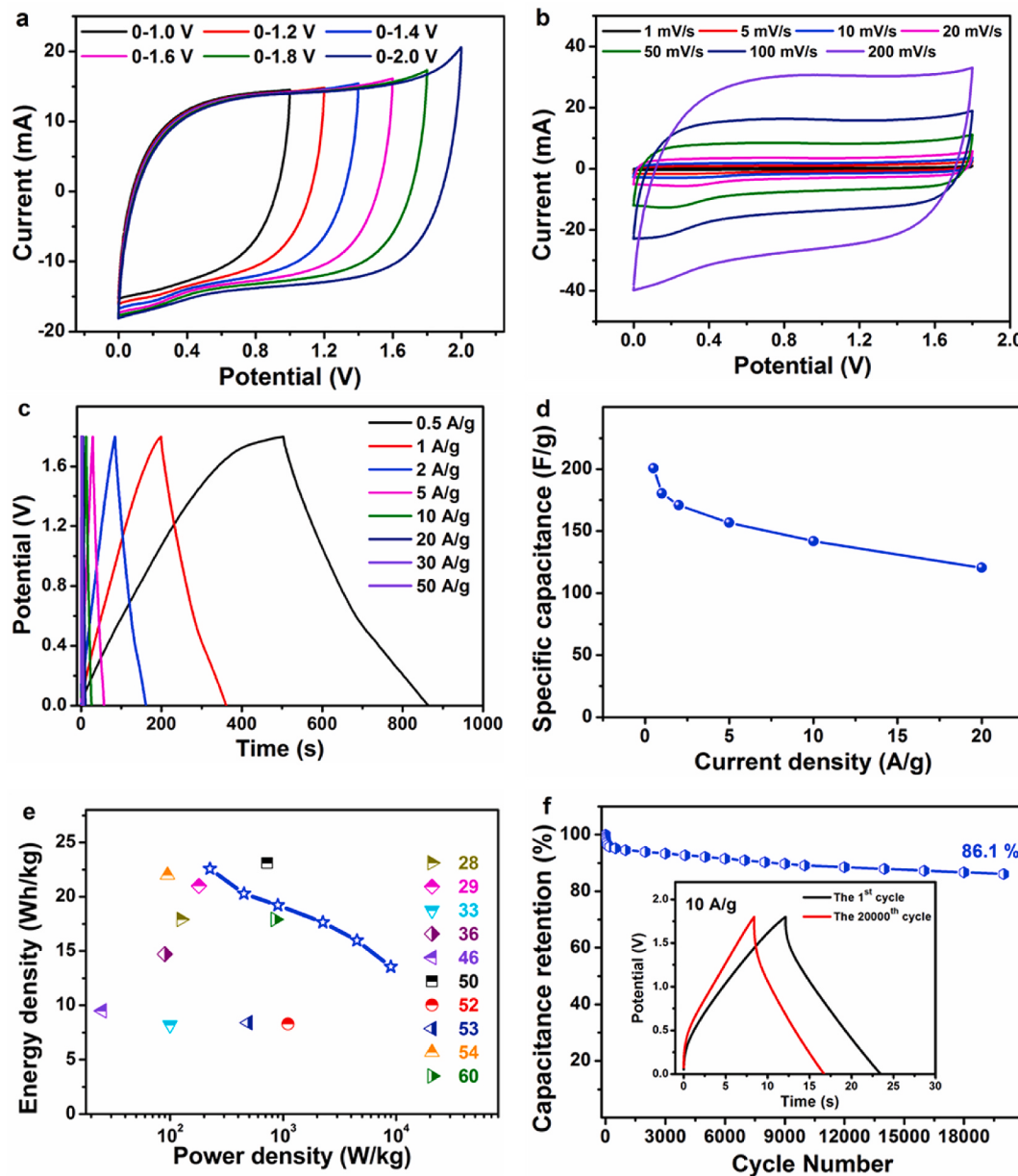


Fig. 8. Electrochemical performance of EW-P-T in 1 M Li_2SO_4 : (a) CV curves at 100 mV s^{-1} with different voltage windows; (b) CV curves at various scan rates; (c) GCD curves at different current densities (d) Specific capacitance vs current density; (e) Ragone plot; (f) Cycle stability at 10 A g^{-1}

features of hierarchical porous carbon materials were favorable for the fast charging/discharging rate in supercapacitors [58,59]. Moreover, the equivalent circuit model was used to analyze the R_{ct} values (Fig. 6b). The simulation result was highly consistent with the Nyquist data, which verified the lowest R_{ct} (0.61Ω) from EW-P-T. In the low-frequency region, the included angle between the straight line of Nyquist plots and $-Z''$ axis was a positive correlation with the diffusion limitation. The straight line of EW-P-T was nearly parallel to the $-Z''$ axis with a small included angle of 3.5° , indicating a typical double-layer capacitive behavior. In addition, the ion diffusion was further quantitatively analyzed by the diffusion coefficient (D). As shown in Equations (3) and (4), there is an inverse relationship between the slope (σ) and the D . The EW-P-T depicted the lowest value of σ (0.3), so it had the highest D among the three samples (Fig. 6c). Furthermore, the Bode plots show the relationship between phase angle and frequency (Fig. 6d). The phase angle of EW-P-T was close to -90° at low frequency, suggesting its ideal capacitive behavior. The time constant (τ_0) derived from the characteristic frequency f_0 at the typical phase angle of -45° for EW-P-T was

0.78 s, which was much shorter than that of EW-T (1.04 s) and EW (2.27 s). These results conjointly demonstrated the excellent ion transport behavior of the EW-P-T due to its hierarchical porous structure and larger ion-accessible SSA.

3.2.2. A two-electrode configuration in 6 M KOH and 1 M Li_2SO_4

Generally two-electrode symmetric supercapacitors were exploited as energy storage for practical application. A two-electrode configuration of EW-P-T was assembled by using 6 M KOH as the electrolyte. Nearly rectangular shapes for CV curves and symmetrical equicircular triangles for GCD curves conjointly suggested an ideal capacitor behavior in supercapacitors (Fig. 7a and 7b). From Fig. 7c, it was seen that the specific capacitance of EW-P-T dropped slowly with the increase of current density from 0.5 to 20 A g^{-1} . The calculated specific capacitance was 252 F g^{-1} at 0.5 A g^{-1} , and high capacitance retention of 81% was remained at 20 A g^{-1} , suggesting the good rate capability. Interestingly, a single EW-P-T based symmetric supercapacitor can successfully light a red LED (Fig. 7c, inset), which vividly suggested the

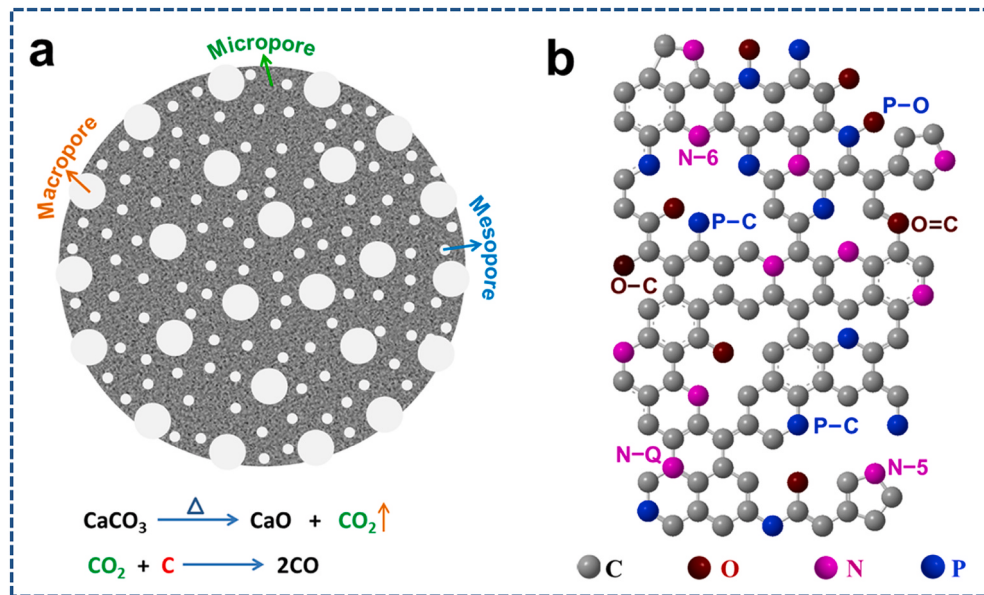


Fig. 9. Schematic illustration of (a) the pore structure and (b) element composition of EW-P-T.

feasibility of EW-P-T in amplified energy storage and output. After the long cycle test for 10000 cycles at a high current density of 10 A g^{-1} , the EW-P-T cell exhibited 90.1% capacitance retention (Fig. 7d). Meanwhile, the Nyquist plot of the inset disclosed a little increase in the ESR after 10000 cycles, further manifesting its actual stability (Fig. 7d, inset).

The electrochemical properties of EW-P-T were further investigated in 1 M Li_2SO_4 neutral electrolyte due to its wider electrochemical window and low corrosiveness. The CV curves of the EW-P-T symmetric supercapacitor were disclosed in Fig. 8a under various voltage windows from 0 to 1.0 to 0–2.0 V with a high scan rate of 100 mV s^{-1} . Apparently, the EW-P-T electrode was stable at the potential window of 0–1.8 V without distinct polarization distortion, suggesting a superior EDLC behavior and outstanding reversibility. Subsequently, Fig. 8b shows the CV curves of the EW-P-T electrode with the potential window of 0–1.8 V at different scan rates. Similarly, it maintained a quasi-rectangular

shape. Meanwhile, a near triangle shape was present in GCD measurements at different current densities from 0.5 to 20 A g^{-1} (Fig. 8c). In Fig. 8d, the calculated capacitances of EW-P-T was 201 F g^{-1} at 0.5 A g^{-1} (also shown in Table S2). Importantly, the assembled EW-P-T based symmetric supercapacitor exhibited a high energy density of 22.6 Wh kg^{-1} at a power density of 225 W kg^{-1} (Fig. 8e), which was higher than that of most previously reported symmetric supercapacitors based on porous carbons [28,29,33,36,46,50,52–54,60]. It still displayed good cycling stability with 86.1% retention after 20000 charging/discharging cycles at the high current density of 10 A g^{-1} in 1 M Li_2SO_4 electrolyte (Fig. 8f). These results revealed that the egg-white derived multi-heteroatom-doped hierarchical porous carbon, EW-P-T, was a promising and desirable electrode material for supercapacitor applications.

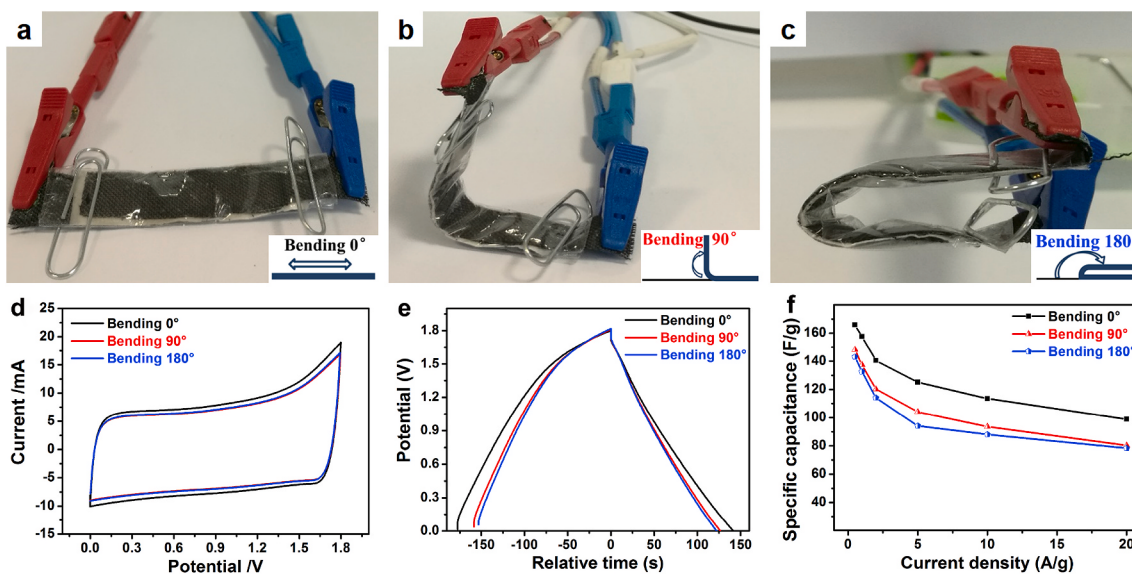


Fig. 10. Electrochemical performances of the flexible device: (a–c) flexible demonstration of flexible devices with the relative illustration for the different bending angle of 0, 90 and 180°, respectively; (d) CV curves with different bending angles at the scan rate of 10 mV s^{-1} ; (e) GCD curves at 0.5 A g^{-1} under various bending status; (f) comparison of specific capacitance over the whole current density.

3.2.3. Analysis of a possible mechanism

As above mentioned, with the help of Na_3PO_4 , a better dispersion of nano- CaCO_3 template in egg white resulted in well-balanced pore size distribution and heteroatom-doped carbon lattice, which made contributions to the promising performances of EW-P-T as supercapacitor electrodes. Firstly, the pore fabricating process from nano- CaCO_3 template was analyzed. According to TGA results for nano- CaCO_3 (the maximum thermal decomposition temperature was approximately 736 °C, shown in Fig. S5), the carbonization of egg white/ Na_3PO_4 /nano- CaCO_3 composites was performed at 800 °C. As shown in Fig. 9a, once the CaCO_3 started to decompose into CaO and CO_2 during annealing, the newly generated CO_2 molecules could directly etch the carbon atoms around them (this CO_2 inner-activation effect could create new pores and enlarge existing pores), so that meso- and micropores were produced. Meanwhile, when CaO nanoparticles were removed by acid treatment, their occupied space was released to form mesopores and macropores (some mesopores were connected to form macropores). The uniform dispersion of nano- CaCO_3 template resulted in homogeneous mesopores and restricted the formation of oversized macropores. As a result, hierarchically porous carbon (micropores and mesopores were dominant while a small number of macropores were bestrewed) was fabricated, which can serve as interfacial active sites to accumulate the transport and diffusion of electrolyte ions, leading to the high capacitance of supercapacitors.

Moreover, the N/O/P co-doped carbon lattice was discussed (Fig. 9b). Generally, the negatively charged N-5 and N-6 groups are beneficial to the pseudo-capacitance of supercapacitors while the N-Q (called graphitic type nitrogen) can improve the conductivity of carbon materials due to its positive effect on electron conduction [61]. The abundant oxygen-containing groups can enhance the wettability of the electrode surface and contribute to high specific capacitance [62,63]. The doping of P in the lattice of the carbon skeleton can induce the distortion and wrinkle in the morphology and further create lots of edge defects [64]. Comparing the P-doped carbon materials in the state of the art, EW-P-T possessed a high level of P doping (Table S1). Although some research groups reported the higher content of P doping [45, 65–67], the content of P-C was much lower than that of EW-P-T. Thus, EW-P-T possessed a high content of N-Q, O-C, and P-C. These advantageous characteristics might trigger the synergistic effect of heteroatoms, resulting in high-performance for supercapacitors.

3.2.4. The application as flexible all-solid-state devices

Flexibility is a crucial parameter for the application of supercapacitors as wearable energy storage devices. A flexible sandwiched supercapacitor with EW-P-T as electrode materials was fabricated by using the 1 M LiCl/PVA gel electrolyte. The electrochemical properties were evaluated with the bending angles of 0°, 90°, and 180° (Fig. 10a–10c). It was seen that the CV curves and GCD curves showed only a little distortion when the device was bent to 90° and 180° (Fig. 10d and 10e). The pattern of specific capacitance vs current density was displayed in Fig. 10f. In comparison with the specific capacitance at 0° bending angle with the same current density of 0.5 A g⁻¹, the flexible supercapacitor could maintain its high capacitance value of 89.4% and 86.3% at 90° and 180°, respectively. Even when the current density increased to 20 A g⁻¹, the capacitance retention at 90° and 180° bending angle were still as high as 80.3% and 78.3%. These results demonstrated that various mechanical bending could not significantly influence its electrochemical behavior, suggesting that EW-P-T based supercapacitor possessed good flexibility and stability. Therefore, it is of great potential to be used in the field of portable energy storage.

4. Conclusions

In summary, N/O/P co-doped 3D hierarchical porous carbon was successfully fabricated from sustainable and low-cost egg-white using Na_3PO_4 assistant dispersion of nano- CaCO_3 template. The as-prepared

porous carbon possessed high specific surface area, hierarchical porous distribution with large pore volume, and heteroatoms co-doped carbon lattice. These unique physicochemical features could enhance interfacial active sites, rapid ion-diffusion channels, and short ion-transport distance, resulting in excellent electrochemical performance as supercapacitor electrodes. More importantly, as an all-solid-state flexible device, it could deliver high mechanical flexibility stability. This work will not only provide a novel, facile, and efficient pathway for high-value utilization of natural biomass but also proposes its application as high-performance supercapacitors and flexible energy storage devices. In the next step, we will continue this research to study the effect of template size on pore structure of carbon materials and their related electrochemical performances. Moreover, we want to extend this template method to synthesize porous carbon materials for other biomass systems.

Author statement

Yanliang Wen and Xiaoguang Liu finished the experiments; Karolina Szymańska, Renata Dobrzyńska helped to characterize the performances. Xin Wen, Xuecheng Chen and Ewa Mijowska supervised to analyze experimental data and revised the manuscript. All authors reviewed the manuscript.

Declaration of competing interest

The authors declare that they have no known competing interests or personal relationships that could have appeared to influence the work reported in this paper.

Acknowledgment

This work was financially supported by the European Union's Horizon 2020 research and innovation program under Marie Skłodowska-Curie Widening Fellowship (MSC-WF, No. 867436) and the National Science Centre, Poland, within the SONATA BIS Project no. UMO-2015/18/E/ST8/00291.

Appendix A. Supplementary data

Supplementary data to this article can be found online at <https://doi.org/10.1016/j.compositesb.2020.108256>.

References

- [1] Dubal DP, Chodankar NR, Kim DH, Gomez-Romero P. Towards flexible solid-state supercapacitors for smart and wearable electronics. *Chem Soc Rev* 2018;47(6): 2065–129.
- [2] Kim JG, Kim HC, Kim ND, Khil MS. N-doped hierarchical porous hollow carbon nanofibers based on PAN/PVP@SAN structure for high performance supercapacitor. *Compos Pt B-Eng*. 2020;186:107825.
- [3] Makino S, Yamauchi Y, Sugimoto W. Synthesis of electro-deposited ordered mesoporous RuO_x using lyotropic liquid crystal and application toward micro-supercapacitors. *J Power Sources* 2013;227:153–60.
- [4] Zhang YX, Sun L, Zhang LK, Li XW, Gu JL, Si HC, et al. Highly porous oxygen-doped NiCoP immobilized in reduced graphene oxide for supercapacitive energy storage. *Compos B Eng* 2020;182:107611.
- [5] Hekmat F, Shahrokhian S, Hosseini H. Direct growth of nickel-cobalt oxide nanosheet arrays on carbon nanotubes integrated with binder-free hydrothermal carbons for fabrication of high performance asymmetric supercapacitors. *Compos B Eng* 2019;172:41–53.
- [6] Li Z, Chen G, Deng J, Li D, Yan T, An Z, et al. Creating sandwich-like Ti₃C₂/TiO₂/rGO as anode materials with high energy and power density for Li-ion hybrid capacitors. *ACS Sustainable Chem Eng* 2019;7(18):15394–403.
- [7] Gastol D, Walkowiak J, Fic K, Frackowiak E. Enhancement of the carbon electrode capacitance by brominated hydroquinones. *J Power Sources* 2016;326:587–94.
- [8] Beguin F, Presser V, Balducci A, Frackowiak E. Carbons and electrolytes for advanced supercapacitors. *Adv Mater* 2014;26(14):2219–51.
- [9] Cai YJ, Luo Y, Xiao Y, Zhao X, Liang Y, Hu H, et al. Facile synthesis of three-dimensional heteroatom-doped and hierarchical egg-box-like carbons derived from moringa oleifera branches for high-performance supercapacitors. *ACS Appl Mater Interfaces* 2016;8(48):33060–71.

- [10] Yan L, Li D, Yan T, Chen G, Shi L, An Z, et al. Confining redox electrolytes in functionalized porous carbon with improved energy density for supercapacitors. *ACS Appl Mater Interfaces* 2018;10(49):42494–502.
- [11] Wulan Septiani NL, Kaneti YV, Fathoni KB, Wang J, Ide Y, Yuliarto B, et al. Self-assembly of nickel phosphate-based nanotubes into two-dimensional crumpled sheet-like architectures for high-performance asymmetric supercapacitors. *Nano Energy* 2020;67:104270.
- [12] Tang J, Salunkhe RR, Zhang H, Malgras V, Ahamad T, Alshehri SM, et al. Bimetallic metal-organic frameworks for controlled catalytic graphitization of nanoporous carbons. *Sci Rep* 2016;6(1):30295.
- [13] Xue DF, Zhu DZ, Duan H, Wang ZW, Lv YK, Xiong W, et al. Deep-eutectic-solvent synthesis of N/O self-doped hollow carbon nanorods for efficient energy storage. *Chem Commun* 2019;55(75):11219–22.
- [14] Preuss K, Tanase LC, Teodorescu CM, Abrahams I, Titirici MM. Sustainable metal-free carbogels as oxygen reduction electrocatalysts. *J Mater Chem A* 2017;5(31):16336–43.
- [15] Xu YX, Shi GQ, Duan XF. Self-assembled three-dimensional graphene macrostructures: synthesis and applications in supercapacitors. *Accounts Chem Res* 2015;48(6):1666–75.
- [16] Ouyang T, Cheng K, Gao YY, Kong SY, Ye K, Wang GL, et al. Molten salt synthesis of nitrogen doped porous carbon: a new preparation methodology for high-volumetric capacitance electrode materials. *J Mater Chem A* 2016;4(25):9832–43.
- [17] Li Y, Henzie J, Park T, Wang J, Young C, Xie H, et al. Fabrication of flexible microsupercapacitors with binder-free ZIF-8 derived carbon films via electrophoretic deposition. *Bull Chem Soc Jpn* 2020;93(1):176–81.
- [18] Zhao J, Jiang YF, Fan H, Liu M, Zhuo O, Wang XZ, et al. Porous 3D few-layer graphene-like carbon for ultrahigh-power supercapacitors with well-defined structure–performance relationship. *Adv Mater* 2017;29(11):8.
- [19] Brandiele R, Picelli L, Pilot R, Causin V, Martucci A, Rizzi GA, et al. Nitrogen and sulfur doped mesoporous carbons, prepared from templating silica, as interesting material for supercapacitors. *ChemistrySelect* 2017;2(24):7082–90.
- [20] Ania CO, Khomenko V, Raymundo-Pinero E, Parra JB, Beguin F. The large electrochemical capacitance of microporous doped carbon obtained by using a zeolite template. *Adv Funct Mater* 2007;17(11):1828–36.
- [21] Cheng PY, Cheng HY, Huang CL, Chen YA, Hsieh CT, Lu SY. N-doped hierarchical continuous hollow thin porous carbon nanostructure for high-performance flexible gel-type symmetric supercapacitors. *ACS Sustainable Chem Eng* 2019;7(20):17020–9.
- [22] Luo EG, Xiao ML, Ge JJ, Liu CP, Xing W. Selectively doping pyridinic and pyrrolic nitrogen into a 3D porous carbon matrix through template-induced edge engineering: enhanced catalytic activity towards the oxygen reduction reaction. *J Mater Chem* 2017;5(41):21709–14.
- [23] Zhou L, Cao H, Zhu SQ, Hou LR, Yuan CZ. Hierarchical micro-/mesoporous N- and O-enriched carbon derived from disposable cashmere: a competitive cost-effective material for high-performance electrochemical capacitors. *Green Chem* 2015;17(4):2373–82.
- [24] Song ZY, Duan H, Zhu DZ, Lv YK, Xiong W, Cao TC, et al. Ternary-doped carbon electrodes for advanced aqueous solid-state supercapacitors based on a "water-in-salt" gel electrolyte. *J Mater Chem* 2019;7(26):15801–11.
- [25] Yan L, Li D, Yan T, Chen G, Shi L, An Z, et al. N,P,S-codoped hierarchically porous carbon spheres with well-balanced gravimetric/volumetric capacitance for supercapacitors. *ACS Sustainable Chem Eng* 2018;6(4):5265–72.
- [26] Yang H, Ye SW, Zhou JM, Liang TX. Biomass-derived porous carbon materials for supercapacitor. *Front Chem* 2019;7:17.
- [27] Liu X, Zhang S, Wen X, Chen X, Wen Y, Shi X, et al. High yield conversion of biowaste coffee grounds into hierarchical porous carbon for superior capacitive energy storage. *Sci Rep* 2020;10(1):3518.
- [28] Li Y, Wang G, Wei T, Fan Z, Yan P. Nitrogen and sulfur co-doped porous carbon nanosheets derived from willow catkin for supercapacitors. *Nano Energy* 2016;19:165–75.
- [29] Zhou L, Cao H, Zhu S, Hou L, Yuan C. Hierarchical micro-/mesoporous N- and O-enriched carbon derived from disposable cashmere: a competitive cost-effective material for high-performance electrochemical capacitors. *Green Chem* 2015;17(4):2373–82.
- [30] Feng H, Hu H, Dong H, Xiao Y, Cai Y, Lei B, et al. Hierarchical structured carbon derived from bagasse wastes: a simple and efficient synthesis route and its improved electrochemical properties for high-performance supercapacitors. *J Power Sources* 2016;302:164–73.
- [31] Li Z, Zhang L, Amirkhiz BS, Tan X, Xu Z, Wang H, et al. Carbonized chicken eggshell membranes with 3D architectures as high-performance electrode materials for supercapacitors. *Adv Energy Mater* 2012;2(4):431–7.
- [32] Qian W, Sun F, Xu Y, Qiu L, Liu C, Wang S, et al. Human hair-derived carbon flakes for electrochemical supercapacitors. *Energy Environ Sci* 2014;7(1):379–86.
- [33] Cheng P, Gao S, Zang P, Yang X, Bai Y, Xu H, et al. Hierarchically porous carbon by activation of shiitake mushroom for capacitive energy storage. *Carbon* 2015;93:315–24.
- [34] Zhu H, Wang X, Yang F, Yang X. Promising carbons for supercapacitors derived from fungi. *Adv Mater* 2011;23(24):2745–8.
- [35] Raymundo-Pinero E, Cadek M, Béguin F. Tuning carbon materials for supercapacitors by direct pyrolysis of seaweeds. *Adv Funct Mater* 2009;19(7):1032–9.
- [36] Shao J, Ma F, Wu G, Dai C, Geng W, Song S, et al. In-situ MgO (CaCO₃) templating coupled with KOH activation strategy for high yield preparation of various porous carbons as supercapacitor electrode materials. *Chem Eng J* 2017;321:301–13.
- [37] Kong L, Liu M, Diao Z, Chen D, Chang X, Xiong Y. Coupling template nanocasting and self-activation for fabrication of nanoporous carbon. *Sci Rep* 2016;6:38176.
- [38] Tian H, Qin J, Hou D, Li Q, Li C, Wu Z-S, et al. General interfacial self-assembly engineering for patterning two-dimensional polymers with cylindrical mesopores on graphene. *Angew Chem Int Ed* 2019;131(30):10279–84.
- [39] Elmouahidi A, Zapata-Benabite Z, Carrasco-Marin F, Moreno-Castilla C. Activated carbons from KOH-activation of argan (*Argania spinosa*) seed shells as supercapacitor electrodes. *Bioresour Technol* 2012;111:185–90.
- [40] Tang T, Chen XC, Meng XY, Chen H, Ding YP. Synthesis of multiwalled carbon nanotubes by catalytic combustion of polypropylene. *Angew Chem Int Ed* 2005;44(10):1517–20.
- [41] Wen X, Gong J, Yu HO, Liu Z, Wan D, Liu J, et al. Catalyzing carbonization of poly(L-lactide) by nanosized carbon black combined with Ni₂O₃ for improving flame retardancy. *J Mater Chem* 2012;22(37):19974–80.
- [42] Wen X, Chen XC, Tian NN, Gong J, Liu J, Rummeli MH, et al. Nanosized carbon black combined with Ni₂O₃ as "universal" catalysts for synergistically catalyzing carbonization of polyolefin wastes to synthesize carbon nanotubes and application for supercapacitors. *Environ Sci Technol* 2014;48(7):4048–55.
- [43] Lin G, Ma R, Zhou Y, Hu C, Yang M, Liu Q, et al. Three-dimensional interconnected nitrogen-doped mesoporous carbons as active electrode materials for application in electrocatalytic oxygen reduction and supercapacitors. *J Colloid Interface Sci* 2018;527:230–40.
- [44] Xu G, Han J, Ding B, Nie P, Pan J, Dou H, et al. Biomass-derived porous carbon materials with sulfur and nitrogen dual-doping for energy storage. *Green Chem* 2015;17(3):1668–74.
- [45] Zhang Y, Sun Q, Xia K, Han B, Zhou C, Gao Q, et al. Facile synthesis of hierarchically porous N/P codoped carbon with simultaneously high-level heteroatom-doping and moderate porosity for high-performance supercapacitor electrodes. *ACS Sustainable Chem Eng* 2019;7(6):5717–26.
- [46] Peng H, Ma G, Sun K, Zhang Z, Yang Q, Lei Z. Nitrogen-doped interconnected carbon nanosheets from pomelo mesocarp for high performance supercapacitors. *Electrochim Acta* 2016;190:862–71.
- [47] Wang J, Tang J, Xu Y, Ding B, Chang Z, Wang Y, et al. Interface miscibility induced double-capillary carbon nanofibers for flexible electric double layer capacitors. *Nano Energy* 2016;28:232–40.
- [48] Zhang H, He X, Gu J, Xie Y, Shui H, Zhang X, et al. Wrinkled porous carbon nanosheets from methylnaphthalene oil for high-performance supercapacitors. *Fuel Process Technol* 2018;175:10–6.
- [49] Wu C, Yang S, Cai J, Zhang Q, Zhu Y, Zhang K. Activated microporous carbon derived from almond shells for high energy density asymmetric supercapacitors. *ACS Appl Mater Interfaces* 2016;8(24):15288–96.
- [50] Tian W, Gao Q, Tan Y, Yang K, Zhu L, Yang C, et al. Bio-inspired beehive-like hierarchical nanoporous carbon derived from bamboo-based industrial by-product as a high performance supercapacitor electrode material. *J Mater Chem A* 2015;3(10):5656–64.
- [51] Zhang H, Noonan O, Huang X, Yang Y, Xu C, Zhou L, et al. Surfactant-free assembly of mesoporous carbon hollow spheres with large tunable pore sizes. *ACS Nano* 2016;10(4):4579–86.
- [52] Chen J, Wei H, Chen H, Yao W, Lin H, Han S. N/P co-doped hierarchical porous carbon materials for superior performance supercapacitors. *Electrochim Acta* 2018;271:49–57.
- [53] Gao F, Qu J, Geng C, Shao G, Wu M. Self-templating synthesis of nitrogen-decorated hierarchical porous carbon from shrimp shell for supercapacitors. *J Mater Chem A* 2016;4(19):7445–52.
- [54] Long C, Chen X, Jiang L, Zhi L, Fan Z. Porous layer-stacking carbon derived from in-built template in biomass for high volumetric performance supercapacitors. *Nano Energy* 2015;12:141–51.
- [55] Li Z, Xu Z, Tan X, Wang H, Holt CMB, Stephenson T, et al. Mesoporous nitrogen-rich carbons derived from protein for ultra-high capacity battery anodes and supercapacitors. *Energy Environ Sci* 2013;6(3):871–8.
- [56] Lu Y, Zhang Q, Lei S, Cui X, Deng S, Yang Y. In situ templating approach to fabricate small-mesopore-dominant S-doped porous carbon electrodes for supercapacitors and Li-ion batteries. *ACS Appl Energy Mater* 2019;2(8):5591–9.
- [57] Du J, Liu L, Yu Y, Zhang Y, Chen A. N-doping carbon sheet and core-shell mesoporous carbon sphere composite for high-performance supercapacitor. *J Ind Eng Chem* 2019;76:450–6.
- [58] Luo J, Ma Q, Gu H, Zheng Y, Liu X. Three-dimensional graphene-polyaniline hybrid hollow spheres by layer-by-layer assembly for application in supercapacitor. *Electrochim Acta* 2015;173:184–92.
- [59] Zhang S, Shi X, Wróbel R, Chen X, Mijowska E. Low-cost nitrogen-doped activated carbon prepared by polyethylenimine (PEI) with a convenient method for supercapacitor application. *Electrochim Acta* 2019;294:183–91.
- [60] An Y, Yang Y, Hu Z, Guo B, Wang X, Yang X, et al. High-performance symmetric supercapacitors based on carbon nanosheets framework with graphene hydrogel architecture derived from cellulose acetate. *J Power Sources* 2017;337:45–53.
- [61] Wang Y, Xuan H, Lin G, Wang F, Chen Z, Dong X. A melamine-assisted chemical blowing synthesis of N-doped activated carbon sheets for supercapacitor application. *J Power Sources* 2016;319:262–70.
- [62] Chen Z, Ye S, Evans SD, Ge Y, Zhu Z, Tu Y, et al. Confined assembly of hollow carbon spheres in carbonaceous nanotube: a spheres-in-tube carbon nanostructure with hierarchical porosity for high-performance supercapacitor. *Small* 2018;14(19):1704015.
- [63] Song S, Ma F, Wu G, Ma D, Geng W, Wan J. Facile self-templating large scale preparation of biomass-derived 3D hierarchical porous carbon for advanced supercapacitors. *J Mater Chem A* 2015;3(35):18154–62.
- [64] Wang X, Liu Y, Wu P. Water-soluble triphenylphosphine-derived microgel as the template towards in-situ nitrogen, phosphorus co-doped mesoporous graphene

- framework for supercapacitor and electrocatalytic oxygen reduction. *Chem Eng J* 2017;328:417–27.
- [65] Zhang M, Yang C, Wang Y, Gao F, Cheng J, Zhang J. High-performance supercapacitor based on nitrogen and phosphorus co-doped nonporous polybenzoxazine-based carbon electrodes. *J Electrochem Soc* 2018;165(14):A3313–20.
- [66] Idris MB, Sai GH, Hemalatha D, Sakthivel G, Devaraj S. The effect of phosphorous doping on the composition and capacitance properties of mesoporous graphitic carbon nitride. *J Electrochem Soc* 2019;166(12):A2409–18.
- [67] Cheng H, Yi F, Gao A, Liang H, Shu D, Zhou X, et al. Supermolecule self-assembly promoted porous N, P Co-doped reduced graphene oxide for high energy density supercapacitors. *ACS Appl Energy Mater* 2019;2(6):4084–91.